Inorganic Chemistry

pubs.acs.org/IC Article

Role of Solvent Coordination in the Multi-electron Redox Cycle of Nickel Diethyldithiocarbamate

Rezoanul Islam, Kallan Blakemore, and Byron H. Farnum*



ACCESS

III Metrics & More

Article Recommendations

SI Supporting Information

ABSTRACT: Nickel(II) diethyldithiocarbamate, Ni^{II}(dtc)₂, is known to undergo a 2e⁻ ligand-coupled electron transfer (LCET) oxidation to form $[Ni^{IV}(dtc)_3]^+$. However, the thermodynamics and kinetics of this 2e⁻ process can be greatly affected by solvent coordination. For low coordinating solvents like acetonitrile and acetone, 2e⁻ oxidation is observed via cyclic voltammetry (CV) at a single potential while stronger coordinating solvents like methanol, N,N-dimethylformamide, dimethyl sulfoxide, and pyridine exhibit a 1e⁻ oxidation wave by formation of $[Ni^{II}(dtc)_2(sol)_x]^+$ intermediates. The decay of these complexes to eventually yield $[Ni^{IV}(dtc)_3]^+$ was monitored as a function of CV scan rate and temperature to extract rate constants and activation parameters. A thorough analysis of activation parameters revealed that ΔH_{app}^+ generally increased with solvent coordination ability, suggesting solvent dissociation was a key factor in the rate limiting step. However, ΔS_{app}^- was found to be negative for all solvents, suggesting an associative mechanism in line with dimer formation with Ni^{II}(dtc)₂ to facilitate ligand exchange. Density function theory calculations supported the competitive nature of dissociative and associative steps. Using these calculations, we propose two paths for decay of $[Ni^{III}(dtc)_2(sol)_x]^+$ species based on the coordination strength of the solvent. These studies point to the ability of solvents to either aid or hinder multielectron LCET reactions.

■ INTRODUCTION

Ligand-coupled electron transfer (LCET) is a key factor which governs multielectron redox chemistry in transition metal complexes. LCET drives these multielectron oxidation and reduction reactions by changes in coordination environment around the metal, which shifts the one-electron redox couples into a state of potential inversion. 1-9 For example, $[Ni^{II}(bpy)_3]^{2+}$, where bpy = 2,2'-bipyridine, experiences a two-electron reduction to $Ni^0(bpy)_2$ at -1.65 V, accompanied by the detachment of one bpy ligand, thus reducing the coordination number from six to four. Another example involves the intramolecular oxidation of Pt(II) to Pt(IV) in the complex $[Pt(tpy)(NCN)]^+$, where tpy is 2,2';6',2"-terperidine and NCN⁻ is 1,3-bis(piperidylmethyl)benzene anion. ¹⁰ In the Pt(II) state, the tethered piperidyl ligands are uncoordinated to the metal center, resulting in a four-coordinate square planar geometry. Oxidation to Pt(IV) coincides with coordination of the piperidyl groups to increase the coordination number from four to six. In all known examples of two-electron LCET reactions, the coordination number around the metal center increases upon oxidation and decreases upon reduction. However, LCET does not always result in multielectron

transfer reactions. Many more examples exist in which ligand association, dissociation, and isomerization reactions simply shift the potentials of one-electron redox couples but do not result in potential inversion. ^{11,12}

Coordinating solvents can also play a significant role in LCET reactions as potential ligands for undercoordinated metal centers, and thus solvent dependent electrochemistry of transition metal complexes have been reported for different ligand environments. ^{13–22} Based on a simple thermochemical cycle, a larger equilibrium constant for solvent coordination in the oxidized state of a metal center versus its reduced state will result in a negative shift of the reduction potential for the solvent bound species with respect to the unbound complex. Simply put, the coordination of solvent can easily be studied by

Received: May 16, 2024 Revised: July 26, 2024 Accepted: July 30, 2024 Published: August 9, 2024





measuring the shift in reduction potential for a given redox couple as a function of the solvent type.

Ni^{II}(dtc)₂, where dtc⁻ is N,N-diethyldithiocarbamate, is a molecule which displays multielectron redox activity controlled by LCET in which Ni^{II}(dtc)₂ is oxidized by two-electrons (2e⁻) to yield [Ni^{IV}(dtc)₃]⁺ (eq 1). The ligand-coupled activity arises from the conversion of the four-coordinate Ni(II) complex to the six-coordinate Ni(IV) complex through addition of a third dtc⁻ ligand. The electrochemistry of this complex and other nickel dithiocarbamate complexes was first studied in acetone (Ac) by Hendrickson and co-workers and in acetonitrile (MeCN) by Lachenal.^{23,24} Both studies showed that while oxidation by 2e⁻ from Ni(II) to Ni(IV) in these solvents occurred at a single potential, the reduction reaction was divided into two 1e⁻ steps at different potentials (Figure 1), corresponding to reduction from Ni(IV) to Ni(III) and Ni(III) to Ni(III).

$$3/2Ni^{II}(dtc)_2 \rightarrow [Ni^{IV}(dtc)_3]^+ + 1/2Ni^{II} + 2e^-$$
 (1)

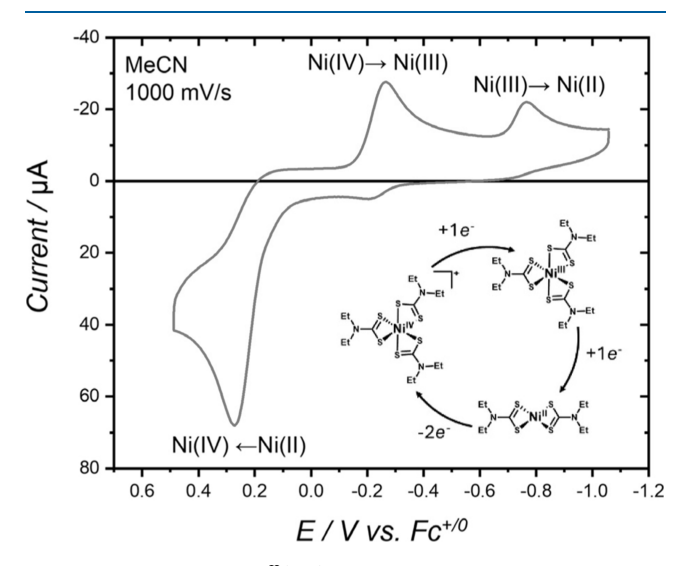


Figure 1. CV of 1 mM $\rm Ni^{II}(dtc)_2$ with 0.1 M TBAPF₆ in **MeCN** at a scan rate of 1000 mV/s. Inset shows redox cycle with chemical structures of $\rm Ni(II)$, $\rm Ni(III)$, and $\rm Ni(IV)$ species.

Our research group has further studied the electrochemistry of $\mathrm{Ni^{II}}(\mathrm{dtc})_2$ in **MeCN** to investigate LCET reactivity as a means of understanding its role in $2\mathrm{e^-}$ redox cycles of transition metal complexes. ^{25–27} Through digital simulations of the cyclic voltammetry (CV) data, we have proposed a thermochemical cycle shown in Figure 2 to summarize the

$$E^{o}_{4} = -0.24 \text{ V} \qquad E^{o}_{3} = -0.71 \text{ V}$$

$$[\text{Ni}^{\text{IV}}(\text{dtc})_{3}]^{+} \longrightarrow \text{Ni}^{\text{III}}(\text{dtc})_{3} \longrightarrow [\text{Ni}^{\text{III}}(\text{dtc})_{3}]^{-}$$

$$\downarrow \uparrow \qquad \qquad \downarrow \downarrow \downarrow \downarrow \downarrow \qquad \qquad \downarrow \downarrow \downarrow \qquad \qquad \downarrow \downarrow \downarrow \qquad \qquad \downarrow \downarrow \downarrow \downarrow \qquad \qquad \downarrow \downarrow \downarrow \qquad \qquad \downarrow \downarrow \downarrow \qquad \qquad \downarrow \downarrow \downarrow \downarrow \qquad \qquad \downarrow \downarrow \downarrow \qquad \qquad \downarrow \downarrow \downarrow \qquad \qquad \downarrow \downarrow \downarrow \downarrow \qquad \qquad \downarrow \downarrow \downarrow \qquad \qquad \downarrow \downarrow \downarrow \qquad \qquad \downarrow \downarrow \downarrow \qquad \qquad \downarrow \downarrow \downarrow \downarrow \downarrow \qquad \qquad \downarrow \downarrow \downarrow \downarrow \downarrow \downarrow \qquad \qquad \downarrow \downarrow \downarrow \downarrow \qquad \qquad \downarrow \downarrow \downarrow \downarrow \downarrow \downarrow \qquad$$

Figure 2. Thermochemical cycle summarizing the nickel-dithiocarbamate redox cycle in **MeCN** solvent. Redox potentials reported versus $Fc^{+/0}$.

overall redox cycle. Oxidation from Ni^{II}(dtc)₂ to [Ni^{IV}(dtc)₃]⁺ proceeds through a formal ECE/DISP process in which 1eoxidation first produces [Ni^{III}(dtc)₂]⁺ (E step, eq 2), followed by conversion to $Ni^{III}(dtc)_3$ (C step, eq 3), and finally one-electron oxidation to $[Ni^{IV}(dtc)_3]^+$ (E step, eq 4). The equilibrium constant for eq 3 was estimated to be K = 0.3based on digital simulations of CV data and it was determined that disproportionation (DISP) of [Ni^{III}(dtc)₂]⁺ and Ni^{III}(dtc)₃ according to eq 5 was the most likely pathway for production of [Ni^{IV}(dtc)₃]⁺, as opposed to direct oxidation of Ni^{III}(dtc)₃ by the electrode. This mechanism is formally classified as DISP1, where the conversion of [Ni^{III}(dtc)₂]⁺ to Ni^{III}(dtc)₃ via eq 3 is rate limiting and the kinetics for disproportionation via eq 5 are much faster. Furthermore, this mechanism is also termed a radical substrate dimerization where the radical $([Ni^{III}(dtc)_2]^+)$ reacts with another equivalent of the substrate $(Ni^{II}(dtc)_2)$ during the rate limiting chemical step.²⁸

In contrast, reduction of [Ni^{IV}(dtc)₃]⁺ upon reversing the polarization proceeds through an EEC pathway in which the stability of Ni^{III}(dtc)₃ results in the second reduction to [Ni^{II}(dtc)₃]⁻ followed by loss of the dtc⁻ ligand to yield Ni^{II}(dtc)₂. Despite the complexities of the overall redox cycle, the chemical reversibility upon cycling between Ni(II) and Ni(IV) oxidation states is remarkably high, resulting in no significant loss of Ni^{II}(dtc)₂ following multiple bulk electrolysis cycles. Recent results from our group have even shown the utility of this redox cycle toward energy storage in redox-flow batteries, where the Ni(IV/II) redox couple underwent 50 cycles over a 24 h period with no significant loss in storage capacity, in addition to application in dye-sensitized solar cells as a redox mediator.^{26,29}

$$Ni^{II}(dtc)_2 \rightarrow [Ni^{III}(dtc)_2]^+ + e^- \qquad E_1^o = 0.25 \text{ V}$$
 (2)

$$[Ni^{III}(dtc)_2]^+ + 1/2Ni^{II}(dtc)_2 \rightarrow Ni^{III}(dtc)_3 + 1/2Ni^{II}$$

 $K = 0.3$ (3)

$$Ni^{III}(dtc)_3 \rightarrow [Ni^{IV}(dtc)_3]^+ + e^- \qquad E_4^o = -0.24 \text{ V}$$
(4)

$$[Ni^{III}(dtc)_2]^+ + Ni^{III}(dtc)_3 \rightarrow Ni^{II}(dtc)_2 + [Ni^{IV}(dtc)_3]^+$$

$$K_{DISP} = 2 \times 10^8$$
 (5)

Much of the thermodynamic and kinetic analysis of the redox cycle was gleaned from studies with added pyridine $(\mathbf{P}y)$ in the electrolyte solution. 25,27 Pyridine was found to coordinate strongly to the $[\mathrm{Ni^{III}}(\mathrm{dtc})_2]^+$ intermediate state to produce five-coordinate $[\mathrm{Ni^{III}}(\mathrm{dtc})_2(\mathbf{P}y)]^+$ and six-coordinate $[\mathrm{Ni^{III}}(\mathrm{dtc})_2(\mathbf{P}y)_2]^+$ species which further slowed the kinetics for conversion to $\mathrm{Ni^{III}}(\mathrm{dtc})_3$. Even with slower kinetics, conversion to $\mathrm{Ni^{III}}(\mathrm{dtc})_3$ and eventually $[\mathrm{Ni^{IV}}(\mathrm{dtc})_3]^+$ was still observed; however, these experiments provided an opportunity to measure the kinetics for decay of the $\mathbf{P}y$ bound species on the CV time scale. $[\mathbf{P}y]$ dependent studies further pointed to pyridine dissociation as a key part of the rate-limiting step.

Our previous studies indicate that coordination of ancillary ligands to the $[Ni^{III}(dtc)_2]^+$ intermediate can have marked effects on the redox cycle, such that MeCN solvent may even play a role in determining electrochemical behavior. Given the weaker coordination strength of MeCN vs Py, we believe that MeCN is able to dissociate more easily from the Ni(III) metal

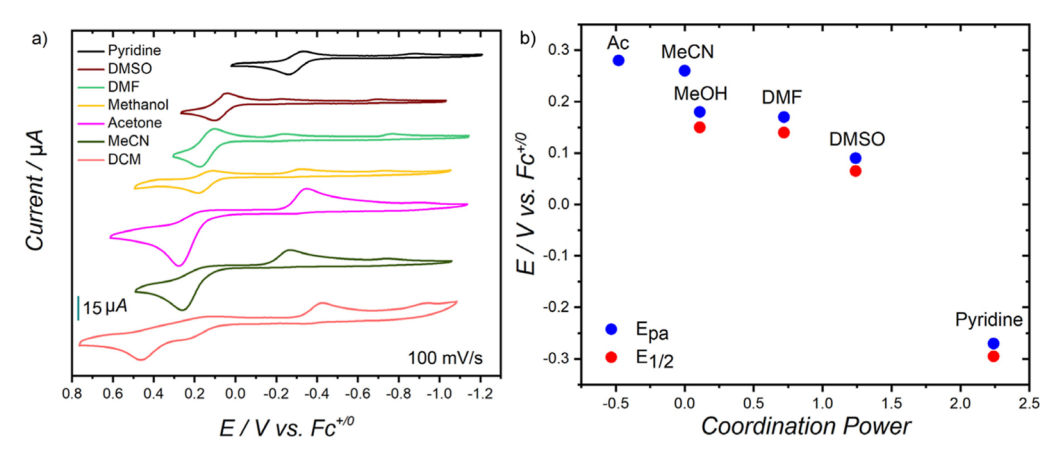


Figure 3. (a) CV data for 1 mM $Ni^{II}(dtc)_2$ at 100 mV/s measured in a range of solvents. In all cases, 0.1 M TBAPF₆ was used as supporting electrolyte. (b) E_{pa} and $E_{1/2}$ versus the solvent coordination power.

center and allow for faster rates of conversion to $[\mathrm{Ni^{IV}(dtc)_3}]^+$ via eqs 3–5, resulting in a 2e⁻ oxidation wave. To test this hypothesis, we report here the electrochemistry of $\mathrm{Ni^{II}(dtc)_2}$ in a range of coordinating and noncoordinating solvents to measure the kinetics for conversion of the solvent (sol) coordinated $[\mathrm{Ni^{III}(dtc)_2(sol)_x}]^+$ to $[\mathrm{Ni^{IV}(dtc)_3}]^+$. Analysis of these kinetics as a function of temperature provided estimates of the apparent activation enthalpies $(\Delta H_{\mathrm{app}}^+)$ and entropies $(\Delta S_{\mathrm{app}}^+)$ for each solvent. Using these values and accompanying density function theory (DFT) calculations, we discuss possible associative and dissociative pathways for conversion of Ni(III) to Ni(IV) along the two-electron path.

■ EXPERIMENTAL SECTION

Synthesis and Characterization of Nill(dtc)₂. Nickel(II) diethyldithiocarbamate was synthesized following a previously described method.^{24,25} Briefly, 2 equiv of sodium diethyldithiocarbamate trihydrate (Sigma, >99.0%) was added to 1 equiv of nickel(II) chloride hexahydrate (Alfa Aesar, 98%) dissolved in Millipore water. A green solid formed immediately and was filtered under vacuum and washed several times with Millipore water and ethanol (200 Proof Pure Ethanol, KOPTEC). The solid was then dried and kept in a vacuum oven at 60 °C until further use.

Electrochemistry. The supporting electrolyte, *n*-tetrabutylammonium hexafluorophosphate (TBAPF₆; Sigma-Aldrich, 98%) was recrystallized from ethanol, then dried under vacuum, and stored in a vacuum oven. A WaveDriver 20 bipotentiostat (Pine Research) was used for electrochemistry experiments with a three-electrode setup which contained a glassy-carbon-disk working electrode (Pine Research, 5 mm diameter), a Ag wire nonaqueous reference electrode (BASi Instruments), and a coiled platinum wire counter electrode (Pine Research). Solvents for electrochemical studies included: acetonitrile (MeCN, Sigma-Aldrich HPLC Plus 99.9%), acetone (Ac, VWR Chemicals 99.5%), methanol (MeOH, VWR Chemicals HPLC grade), *N,N*-dimethylformamide (DMF, Sigma-Aldrich anhydrous 99.8%), dimethyl sulfoxide (DMSO, Sigma-Aldrich anhydrous 99.9%), pyridine (Py, Sigma-Aldrich anhydrous 99.9%), dichloromethane (DCM, VWR Chemicals 99.5%).

A unique reference electrode was prepared for each solvent which contained a Ag wire immersed in a solution of 0.1 M TBAPF $_6$ in the respective solvent in order to minimize liquid/liquid junction potentials at the reference electrode frit. The addition of a Ag $^+$ salt to the reference electrode was avoided because leakage of Ag $^+$ ions into the main electrochemical cell has been observed to result in disturbances of the Ni^{II}(dtc) $_2$ electrochemistry. Reference electrodes were calibrated before and after each experiment using ferrocene (Fc; Alfa Aesar, 99%) as an external standard.

All electrochemistry experiments were performed with 0.1 M TBAPF₆ in the respective solvents with continuous purging of N₂ for bubbling the solution before CV scans and the cannula was kept above the solution in the cell while performing CV scans. Before each experiment, the glassy carbon working electrode was polished with 0.05 µm water-alumina slurry (Allied High Tech Products Inc., deagglomerated). Temperature control of the electrolyte solution was achieved using a jacketed electrochemical cell (Pine Research) connected to a temperature-controlled water circulator (Julabo, model 601F). A thermometer was placed inside the electrochemical cell to make sure the temperature inside the solution matched the desired temperature. In all CV experiments, the potential was cycled from an initial potential of -1.1 V vs $Fc^{+/0}$ in a positive direction for a total of three cycles. The data shown throughout the text and Supporting Information is that of the third cycle. All experiments were performed after compensating for the internal solution resistance. All experiments were performed in triplicate with averages and standard deviations of kinetic measurements.

Electrochemical Modeling. CV simulations for model working curves and experimental data were generated using DigiElch 8 software. Complete details are provided in the Supporting Information.

DFT Calculations. Chemical structures were first modeled using Avogadro software and then optimized using Gaussian 16^{30} software with a 6-31+G* basis set, and MN15 functional. A self-consistent reaction field (SCRF) with SMD option was used to model different solvent environments. Optimizations were performed with the Alabama Supercomputer.

■ RESULTS AND DISCUSSION

Figure 3a shows cyclic voltammograms (CVs) obtained for 1 mM Ni^{II}(dtc)₂ with 0.1 M TBAPF₆ in a range of solvents. Here, the anodic and cathodic peak positions as well as the reversibility of each redox wave changes in each solvent environment. Table S1 provides a summary of all peak potentials and peak currents for each solvent at a scan rate of ν = 100 mV/s. The solvent dependence for the oxidation of Ni^{II}(dtc)₂ is proposed to be due to the coordination ability of the solvent, with more strongly coordinating solvents producing a larger negative shift in the anodic peak. This has been discussed in detail in our previous work on titrations of different pyridine derivatives where the redox wave shifted according to the concentration of the pyridine and the equilibrium constant for coordination to the [Ni^{III}(dtc)₂]⁺ intermediate.^{25,27} A similar proposition is presented here, where any solvent may coordinate to [Ni^{III}(dtc)₂]⁺ and shift the redox wave according to its binding strength. Equations 6–8 describes this process whereby $E_{\rm sol}$ represents the solvent-

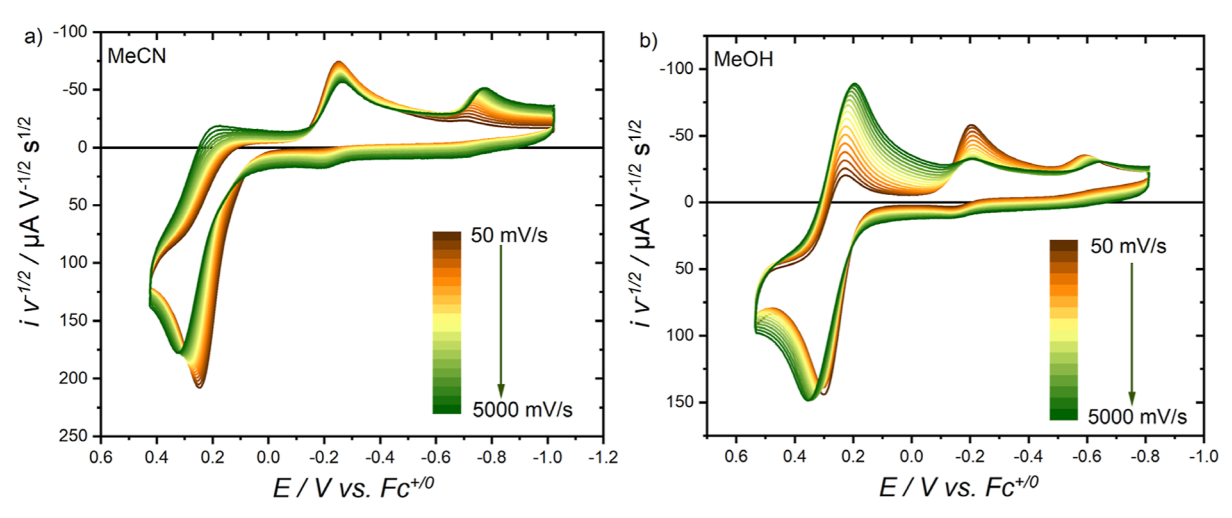


Figure 4. Scan rate normalized CVs of 1 mM Ni^{II}(dtc), in (a) MeCN and (b) MeOH at 25 °C. 0.1 M TBAPF₆ used as supporting electrolyte.

shifted redox potential and E^{o} is the standard potential for the $[Ni^{III}(dtc)_2]^+/Ni^{II}(dtc)_2$ couple in the absence of solvent coordination. Given that some solvents produce an irreversible wave, the anodic peak potential (E_{pa}) was used to monitor this shift. Figure 3b shows a plot of E_{pa} (and $E_{1/2}$ when available) versus the coordination power of each solvent as determined by Munakata et al. for coordination to Ni(II) ions.³¹ Coordination power is a logarithmic ratio of the coordination ability of a given solvent relative to that of MeCN with values of -0.48 (Ac), 0.00 (MeCN), 0.11 (MeOH), 0.72 (DMF), 1.24 (DMSO), and 2.24 (Py). This scale is qualitatively similar to the donor number scale developed by Gutmann for solvent coordination to the hard acid antimony(V) chloride,³² but is more specific to the intermediate acidity of nickel ions. For comparison, Figure S1 shows $E_{\rm pa}$ and $E_{\rm 1/2}$ plotted versus the solvent donor number. The observation that E_{pa} (and $E_{1/2}$) was shifted to more negative potentials with increased coordination power is expected based on the solvent coordination argument.

$$[\operatorname{Ni}^{\operatorname{III}}(\operatorname{dtc})_{2}]^{+} + x\operatorname{sol} \to [\operatorname{Ni}^{\operatorname{III}}(\operatorname{dtc})_{2}(\operatorname{sol})_{x}]^{+} \qquad K_{\operatorname{sol}} \quad (6)$$

$$Ni^{II}(dtc)_2 + xsol \rightarrow [Ni^{III}(dtc)_2(sol)_x]^+ + e^- \qquad E_{sol}$$
(7)

$$E_{\text{sol}} = E^{\text{o}} - (RT/F) \ln(K_{\text{sol}}[\text{sol}]^{x})$$
(8)

In the case of noncoordinating **DCM**, we observed two irreversible oxidation waves in sequence. Based on the thermochemical cycle in Figure 2, we believe this result indicates oxidation along the bottom horizontal path with the first oxidation being consistent with oxidation at the standard value E° represented in eq 8. Although this peak is highly irreversible, a small shoulder cathodic peak was observed at $E_{\rm pc}$ = 0.12 V, resulting in an $E_{1/2}$ = 0.18 V vs Fc^{+/0}. The similarity of this value to oxidation peaks in **MeCN** and **Ac** suggests weak binding of these solvents. Notably, the value of E_1° = 0.25 V given in eq 2 and Figure 2 was derived from simulations of the CV data in **MeCN** solvent and is very close to the $E_{1/2}$ = 0.18 V determined for **DCM** solvent.²⁵

The second oxidation peak observed in **DCM** is proposed to result in a doubly oxidized $[Ni(dtc)_2]^{2+}$ species. We hesitate to assign $[Ni(dtc)_2]^{2+}$ to a Ni(IV) oxidation state as all other literature examples of Ni(IV) have exhibited high coordination numbers with only a few exceptions of organometallic four-coordinate species. 33,34 It is more likely that oxidation of the

sulfur atoms on the dtc⁻ ligand or a combination of metal and ligand-based redox activity is responsible for this wave. Regardless, the doubly oxidized species still appears to convert to the ultimate [Ni^{IV}(dtc)₃]⁺ as evidenced by the cathodic waves at -0.43 and -0.92 V, which are similar to those observed in other solvents when [Ni^{IV}(dtc)₃]⁺ was produced. Therefore, the oxidation mechanism in DCM appears to be EEC, as opposed to the ECE mechanism established for MeCN. We note that DCM was the most difficult solvent to achieve reproducible results and while it serves as an interesting counterpoint to the other coordinating solvents, we did not pursue further studies on the kinetics of Ni(III) intermediates as was done for other solvents.

The reversibility of the solvent coordinated redox wave also trended toward higher reversibility with more strongly coordinating solvents. The new cathodic peak which emerged in the case of MeOH, DMF, DMSO, and Py is assigned to reduction of $[\mathrm{Ni^{II}(dtc)_2(sol)_x}]^+$ back to $\mathrm{Ni^{II}(dtc)_2}$ coupled with dissociation of the solvent. For irreversible oxidation peaks like those observed in MeCN and Ac, we believe the solvent bound $\mathrm{Ni(III)}$ intermediates are too short-lived to be observed at this scan rate, and thus quickly convert to $[\mathrm{Ni^{IV}(dtc)_3}]^+$.

Figure 4 shows scan rate dependent CV data for 1 mM $Ni^{II}(dtc)_2$ in **MeCN** and **MeOH** from v = 50 to 5000 mV/s at 25 °C. Note that the current axis has been normalized by $v^{1/2}$ to better show the changes in reversibility of the solvent coordinated Ni(III/II) wave as a function of scan rate. In MeCN, a small reduction peak at 0.25 V appeared at high scan rates, assigned to reduction of the solvent bound $[Ni^{III}(dtc)_2(MeCN)_x]^+$ species. Likewise a slight decrease in the current observed at high scan rates for the Ni(IV/III) reduction at -0.28 V is due to a lower concentration of [Ni^{IV}(dtc)₃]⁺ being produced at high scan rates. These observations are replicated and magnified in the case of MeOH, where the cathodic peak current near 0.25 V assigned to reduction of $[Ni^{III}(dtc)_2(MeOH)_x]^+$, is much larger than was observed for MeCN and clearly contains an inverse relationship as a function of scan rate with respect to the cathodic peak current for the Ni(IV/III) wave at -0.20 V.

These data reinforce our previous results from Py titration studies in MeCN in which Py coordination to the Ni(III) intermediate decreased the rate of $[Ni^{IV}(dtc)_3]^+$ formation. Here, the result is shown to be general for any coordinating

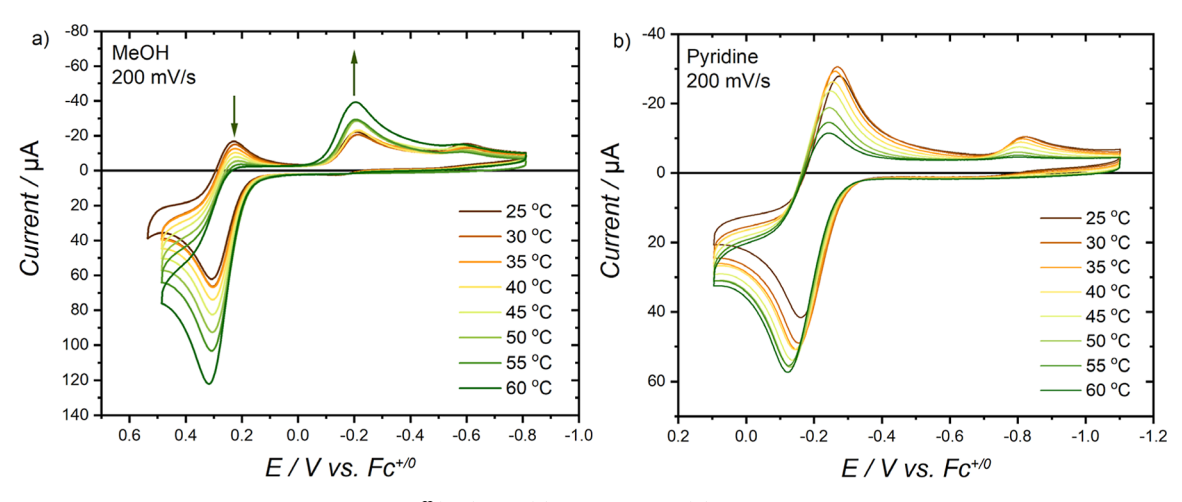


Figure 5. Temperature dependent CVs of 1 mM Ni^{II}(dtc)₂ in (a) MeOH and (b) Py at $\nu = 200$ mV/s. 0.1 M TBAPF₆ used as supporting electrolyte.

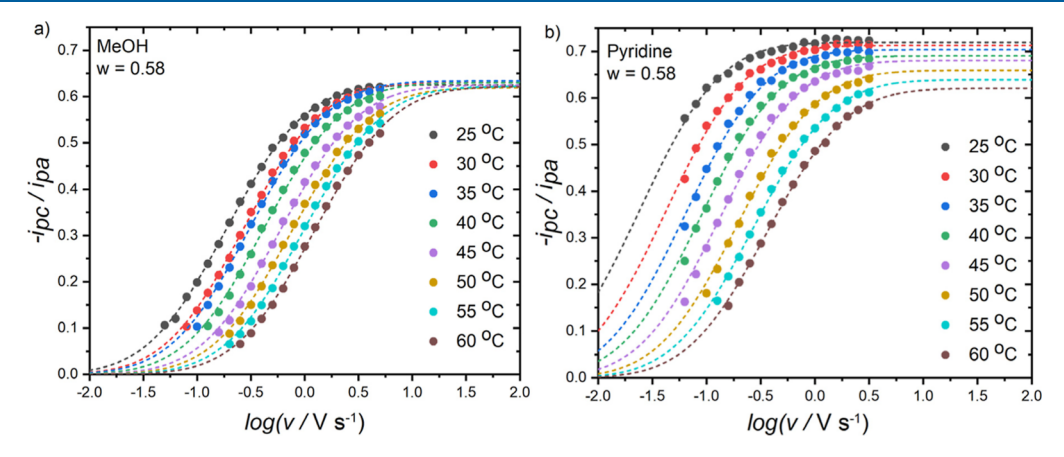


Figure 6. $-i_{pc}/i_{pa}$ vs $\log(v)$ plots used for determination of k_{obs} in (a) MeOH and (b) Py. Dashed lines indicated fits to eq 9 with k_{obs} determined from eq 10.

solvent with the attenuated rate dependent on the solvent coordination ability. In our previous work, we measured the observed rate constant (k_{obs}) using the ratio of the peak currents $(-i_{pc}/i_{pa})$ for the solvent coordinated Ni(III/II) redox wave as a function of scan rate. In the present study, we employed a similar strategy to measure $k_{
m obs}$ in pure solvents as a function temperature to extract activation parameters related to each solvent. Temperature dependent CV experiments were performed in triplicate using 5 °C intervals from 25-60 °C, except for Ac (25-50 °C), with varied scan rate (Figures S2-S7). For all solvents, an increase in temperature corresponded with a decrease in reversibility of the $[Ni^{III}(dtc)_2(sol)_x]^+/$ $Ni^{II}(dtc)_2$ redox couple, as indicated by a decrease in $|i_{pc}|$ and increase in i_{pa} , thus lowering the $-i_{pc}/i_{pa}$ ratio. Figure 5 shows representative data for MeOH and pyridine at v = 200 mV/sfor the range of temperatures studied. Similar figures for other solvents are presented in Figure S8. In the case of MeOH, the downward arrow shown in the figure is meant to indicate that the cathodic current for reduction of [Ni^{III}(dtc)₂(MeOH)_x]⁺ decreased at higher temperatures while the upward arrow indicates cathodic current for reduction of [Ni^{IV}(dtc)₃]⁺ increased. Data for DMF and DMSO show similar results and reinforce the assignment of a kinetic process which converts $[Ni^{III}(dtc)_2(sol)_x]^+$ into $[Ni^{IV}(dtc)_3]^+$ on the CV time scale. In the case of Py, the solvent coordinated Ni(III/II) redox couple is shifted negatively to the point of overlapping

the [Ni^{IV}(dtc)₃]⁺ reduction peak; however, our previous results for low [Py] in MeCN show similar results as MeOH, DMF, and DMSO, in which the two reduction peaks are separated and a clear inverse relationship can be observed. 25,27

Figure 6 shows representative plots of $-i_{pc}/i_{pa}$ vs $\log(\nu)$ for (a) MeOH and (b) Py at different temperatures. Similar data for DMF and DMSO are shown in Figures S9. Note that $-i_{pc}$ and i_{pa} were extracted from raw peak currents without subtraction of nonfaradaic background currents. We have found that subtracting nonfaradaic currents can be highly subjective depending on how the linear extrapolation of nonfaradaic current is performed, especially in the case of the return wave $(-i_{pc})$. The end result is that $-i_{pc}/i_{pa}$ maxima are well below the expected value of 1 even though ratios observed at high scan rates reach near constant values, consistent with reversible behavior. Although temperature and scan rate dependent CV data were collected for MeCN and Ac, the irreversibility of their redox waves precluded the determination of $-i_{pc}/i_{pa}$ ratios that could be analyzed over a wide range of scan rates.

Figure 6 shows that the $-i_{\rm pc}/i_{\rm pa}$ ratio increased with higher scan rates. This result is consistent with an ECE mechanism in which the $-i_{\rm pc}/i_{\rm pa}$ ratio represents the chemical reversibility of the first E-step. Higher scan rates thus result in a more appreciable reduction of $[{\rm Ni^{III}}({\rm dtc})_2({\bf sol})_x]^+$ by limiting the time for the intermediate C-step to occur. Each temperature

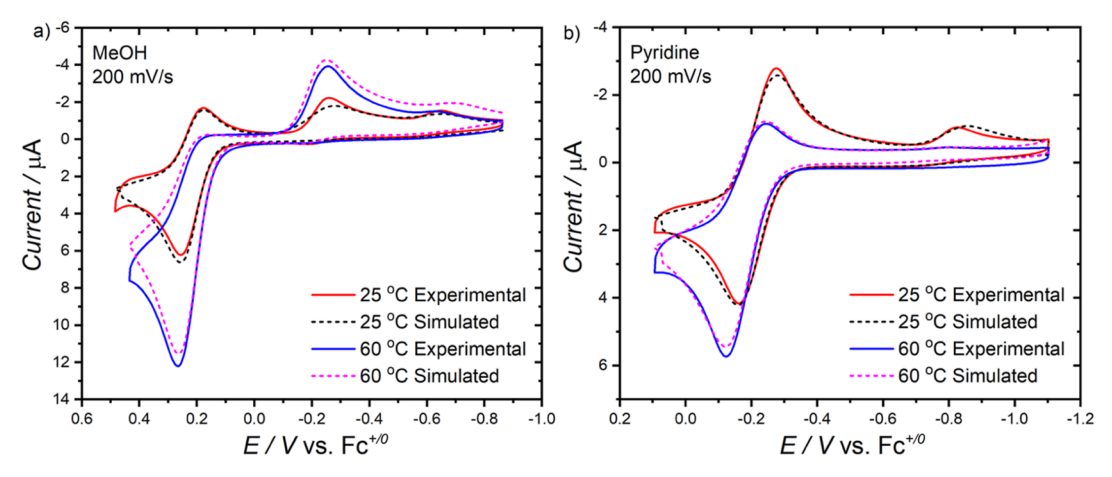


Figure 7. Comparison of experimental and simulated CV data for 1 mM Ni^{II}(dtc)₂ collected at 25 and 60 °C with ν = 200 mV/s and 0.1 M TBAPF₆ in (a) **MeOH** and (b) **Py**.

yielded a different sigmoidal curve for the increase in current ratio with scan rate and thus reflects a change in the $k_{\rm obs}$ for the C-step. Higher $k_{\rm obs}$ values are represented by curves which are shifted toward higher scan rates.

Observed rate constants for each temperature were calculated by two methods: (1) an empirical fitting analysis of the $-i_{\rm pc}/i_{\rm pa}$ curve and (2) digital simulations of CV data. Each of these methods represents different levels of rigor required for extraction of $k_{\rm obs}$ values with pros and cons to each approach. As will be discussed below, the $-i_{\rm pc}/i_{\rm pa}$ analysis offers a quick way to measure $k_{\rm obs}$ with little, but important, assumptions about the redox system. On the other hand, CV simulations provide a thorough analysis of the entire voltammogram; however, they require multiple chemical reactions to properly execute, each with their own list of floating parameters and thus multiple ways to achieve a best fit.

In our previous work, a working curve analysis of the $-i_{pc}/i_{pa}$ curve was employed to extract values of $k_{\rm obs}$ for different concentrations of Py. A working curve was developed from digital simulations of CVs collected in MeCN as a function of scan rate using a standard rate constant $(k_{obs} = 1 \text{ s}^{-1})$ for the C-step reaction. The working curve was then shifted horizontally along the x-axis until visual alignment with the data points was achieved. The amount to which the data was shifted was then used to calculate $k_{\rm obs}$. This method is common to the field of mechanistic electrochemistry; however, the fitting procedure is inherently subjective as it does not employ a statistical, iterative fitting analysis and relies on the scientist to make their best judgment on the quality of the fit. Furthermore, unique working curves must also be generated for different mechanisms (e.g., ECE, DISP1, and DISP2), potential ranges, and electron transfer rate constants. As an example, we generated 15 working curves for each of these differences and found that while the curvatures of the $-i_{
m pc}/i_{
m pa}$ vs log(v) plots were constant for a DISP1 mechanism, the maximum current ratio achieved at high scan rates was highly dependent on the potential range and electron transfer rate constants. These latter terms are subjective to the solvent and temperature for each experiment and thus make it difficult to generate unique working curves for each condition.

As an alternative approach, we fit the $-i_{\rm pc}/i_{\rm pa}$ data using eq 9, which modeled the sigmoidal shape of the data and allowed for iterative fitting methods to be applied. This empirical analysis resulted in statistical values of the $-i_{\rm pc}/i_{\rm pa}$ maximum

(max), the inflection point (m), and the width (w). The dashed lines overlaid on the data in Figure 6 represent fits to eq 9 where the max and m values were allowed to float to find best-fit conditions while the width was held constant at w=0.58. Comparisons of eq 9 with working curves derived for specific mechanisms found that the width was constant for a DISP1 mechanism with w=0.58 (Figure S10). Our analysis of the simulated working curves using eq 9 further found that changes to the potential range (Figure S11), caused by shifts in $E_{\rm pa}$ with temperature and scan rate, was the most likely source of changes in max with temperature, as observed for Py and DMF. These changes could introduce errors of as much as 20% in the measurement of $k_{\rm obs}$.

$$\frac{-i_{\rm pc}}{i_{\rm pa}} = \frac{max}{2} \left[1 + \operatorname{erf} \left(\frac{\log(v) - m}{w\sqrt{2}} \right) \right] \tag{9}$$

$$k_{\rm obs} = \frac{\lambda_m F \nu_m}{RT} = \frac{\lambda_m F 10^m}{RT} \tag{10}$$

The observed rate constants were then calculated using eq 10, where F is Faraday's constant, R is the ideal gas constant, T is temperature, m is the inflection point obtained from the fit, and λ_m is the kinetic parameter at the inflection point. The kinetic parameter for the C-step of an DISP1 mechanism is defined as $\lambda = k_{\text{obs}}RT/F\nu$. This value changes with scan rate and reflects the extent to which the C-step proceeds. For high scan rates, λ is small and thus the C-step is less significant, resulting in more reversible Ni(III/II) behavior. For low scan rates, λ is large and the C-step is more prominent, resulting in irreversible behavior. Given that the m value corresponds to a specific scan rate (v_m) at the inflection point [i.e., $m = \log(v_m)$], a value of $\lambda_m = 0.089$ can be calculated from fits of the standard working curve to eq 9 (See Supporting Information for further details). Provided that the general mechanism does not change with temperature, and thus the curvature of the $-i_{pc}/i_{pa}$ data remains constant, then $\lambda_m = 0.089$ will be applicable for any

Digital simulations of the CV data as a function of temperature and scan rate were also performed using a DISP1 mechanism. The methods for these simulations are described further in the Supporting Information. Figure 7 shows simulated CV data (dashed lines) overlaid on experimental data (solid lines) obtained in MeOH and Py at 25 and 60 $^{\circ}$ C with ν = 200 mV/s. Figures S12 show similar

figures for DMF, DMSO, MeCN, and Ac. In all cases, digital simulations of the data provided visual agreement with the experimental CV data. Importantly, this agreement was achieved over a wide potential range and contained multiple redox features, not just the solvent-coordinated Ni(III/II) redox feature.

Table 1 provides a summary of k_{obs} values determined in **MeOH** and **Py** for the C-step of the DISP1 mechanism using

Table 1. Observed Rate Constants Measured for Conversion of $[Ni^{III}(dtc)_2(sol)_x]^+$ to $[Ni^{IV}(dtc)_3]^+$ in MeOH and Py Solvents Using $-i_{pc}/i_{pa}$ Analysis^a and CV Simulations^b

temp/°C	MeOH $k_{\rm obs}/{\rm s}^{-1}$		pyridine $k_{\rm obs}/{\rm s}^{-1}$	
	$-i_{\rm pc}/i_{\rm pa}$	CV simulation	$-i_{\rm pc}/i_{\rm pa}$	CV simulation
25	0.78 ± 0.09	0.67 ± 0.02	0.08 ± 0.01	0.14 ± 0.01
30	0.98 ± 0.04	0.78 ± 0.02	0.13 ± 0.01	0.21 ± 0.02
35	1.13 ± 0.07	0.94 ± 0.02	0.19 ± 0.02	0.29 ± 0.02
40	1.48 ± 0.08	1.22 ± 0.03	0.29 ± 0.01	0.41 ± 0.01
45	2.01 ± 0.05	1.52 ± 0.03	0.42 ± 0.02	0.58 ± 0.04
50	2.62 ± 0.11	1.96 ± 0.06	0.61 ± 0.01	0.68 ± 0.07
55	3.51 ± 0.24	2.54 ± 0.13	0.83 ± 0.04	0.72 ± 0.04
60	4.65 ± 0.38	3.38 ± 0.12	1.12 ± 0.03	0.82 ± 0.03

^aError reflects the standard deviation from three separate experiments. ^bError reflects the standard error of the fit for simulation of a single experiment.

 $-i_{\rm pc}/i_{\rm pa}$ analysis of the Ni(III/II) feature and CV simulations. Rate constants for DMF, DMSO, MeCN, and Ac are shown in Table S5. Rate constants obtained from $-i_{pc}/i_{pa}$ analysis represent the average from three, independent experiments in which scan rate dependent CVs were collected over a range of temperatures for each experiment. Rate constants obtained from CV simulations were obtained from analyzing a single set of experimental data. The data agree remarkably well at lower temperatures with the $-i_{\rm pc}/i_{\rm pa}$ analysis estimating slightly larger k_{obs} values at higher temperatures. Overall, the agreement between the two methods shows that the $-i_{
m pc}/i_{
m pa}$ analysis is an accurate and simple method for estimating k_{obs} without the need for digital simulations of the entire CV. Notably, the CV simulations also require a total of six reactions to achieve the DISP1 mechanism, all of which come with their own equilibrium constants and rate constants that increases the error in the resulting $k_{\rm obs}$. Likewise, the generation of a working curve also requires simulating CV data based on key assumptions about the reaction steps. These results show that by using the empirical analysis of $-i_{pc}/i_{pa}$ data with eqs 9 and 10, $k_{\rm obs}$ can be obtained with fewer assumptions. Nonetheless, the $-i_{pc}/i_{pa}$ analysis is inherently limited to the ability to quantify the current ratio in an accurate manner. Such requirements precluded us from being able to analyze data from MeCN and Ac, whereas CV simulations were able to estimate $k_{\rm obs}$ given the global nature of the fitting method.

 simulations. Table 2 provides a summary of these apparent activation parameters.

$$\ln\left(\frac{k_{\text{obs}}}{T}\right) = \ln\left(\frac{k_{\text{B}}}{h}\right) + \frac{\Delta S_{\text{app}}^{\ddagger}}{R} - \frac{\Delta H_{\text{app}}^{\ddagger}}{R} \left(\frac{1}{T}\right) \tag{11}$$

We stress the apparent nature of these activation parameters because of the inherent complexity of the C-step for the DISP1 mechanism. This mechanism is written formally in eqs 12-14 to aid in the discussion. From the C-step shown in eq 13, it is clear that solvent dissociation from $[Ni^{III}(dtc)_2(sol)_x]^+$ is required for the reaction to proceed; however, the addition of a third dtc ligand is also necessary to produce Ni^{III}(dtc)₃. These reactions may occur sequentially or simultaneously, and thus the rate limiting step for eq 13 is not straightforward. Inspecting the activation parameters, the apparent enthalpy of activation increased generally with the expected coordination strength of the solvent, although Py yielded a lower $\Delta H_{\rm app}^{\ \ \dagger}$ than **DMSO** for both $k_{\rm obs}$ fitting methods. This increase in $\Delta H_{\rm app}^{\ \ \dagger}$ with coordination strength supports the dissociative requirement of solvent being removed from $[Ni^{III}(dtc)_2(sol)_x]^+$. However, the ΔS_{app}^+ values were found to indicate an overall associative mechanism for the rate limiting step in all solvents for both methods in which k_{obs} was determined. This result suggests that association with Ni^{II}(dtc)₂ must also be involved.

$$Ni^{II}(dtc)_2 + xsol \rightarrow [Ni^{III}(dtc)_2(sol)_x]^+ + e^-$$

E-step (12)

$$[\mathrm{Ni^{III}(dtc)_2(sol)_x}]^+ + 1/2\mathrm{Ni^{II}(dtc)_2} \rightarrow \mathrm{Ni^{III}(dtc)_3}$$
$$+ 1/2\mathrm{Ni^{II}(sol)_x} \qquad \text{C-step} \qquad (13)$$

$$[Ni^{III}(dtc)_{2}(sol)_{x}]^{+} + Ni^{III}(dtc)_{3} \rightarrow Ni^{II}(dtc)_{2}$$

$$+ [Ni^{IV}(dtc)_{3}]^{+} + xsol \qquad DISP \qquad (14)$$

Figure 9 shows trends in the $\Delta H_{\rm app}^{\ \ \dagger}$ and $\Delta S_{\rm app}^{\ \ \dagger}$ vs solvent coordination power. As previously discussed, the coordination power scale was developed specifically for solvent coordination to nickel.³¹ Similar plots using the Gutmann donor number for parameters follow a similar trend, regardless of the solvent coordination scale, increasing generally with coordination power but also showing a surprising decrease for Py. As stated above, the increase in $\Delta H_{\rm app}^{\pm}$ with coordination power is expected for solvent dissociation and would be expected to trend in a more linear fashion if solvent dissociation were the sole rate limiting step. The increase in $\Delta S_{\rm app}^{\ \ \dagger}$ with coordination power suggests broadly that weaker coordinating solvents allow for a more associative mechanism to proceed while more strongly coordinating solvents trend in the dissociative direction. The balance of these two parameters suggests that there is no single rate limiting step in the reaction mechanism. Instead, solvent dissociation and Ni^{II}(dtc)₂ association may occur with similar activation energies and therefore k_{obs} is a mathematical combination of their individual rate constants. Interestingly, the best trend for these activation parameters is when $\Delta S_{\rm app}^{\dagger}$ is plotted versus $\Delta H_{\rm app}^{\dagger}$ for the range of solvents (Figure 10). Here, a linear trend is observed where a smaller $\Delta H_{\rm app}^{\ \ \dagger}$ resulted in a more associative $\Delta S_{\rm app}^{\ \ \dagger}$ and a larger $\Delta H_{\rm app}^{\ \ \dagger}$ resulted in a less associative $\Delta S_{\rm app}^{\ \ \dagger}$.

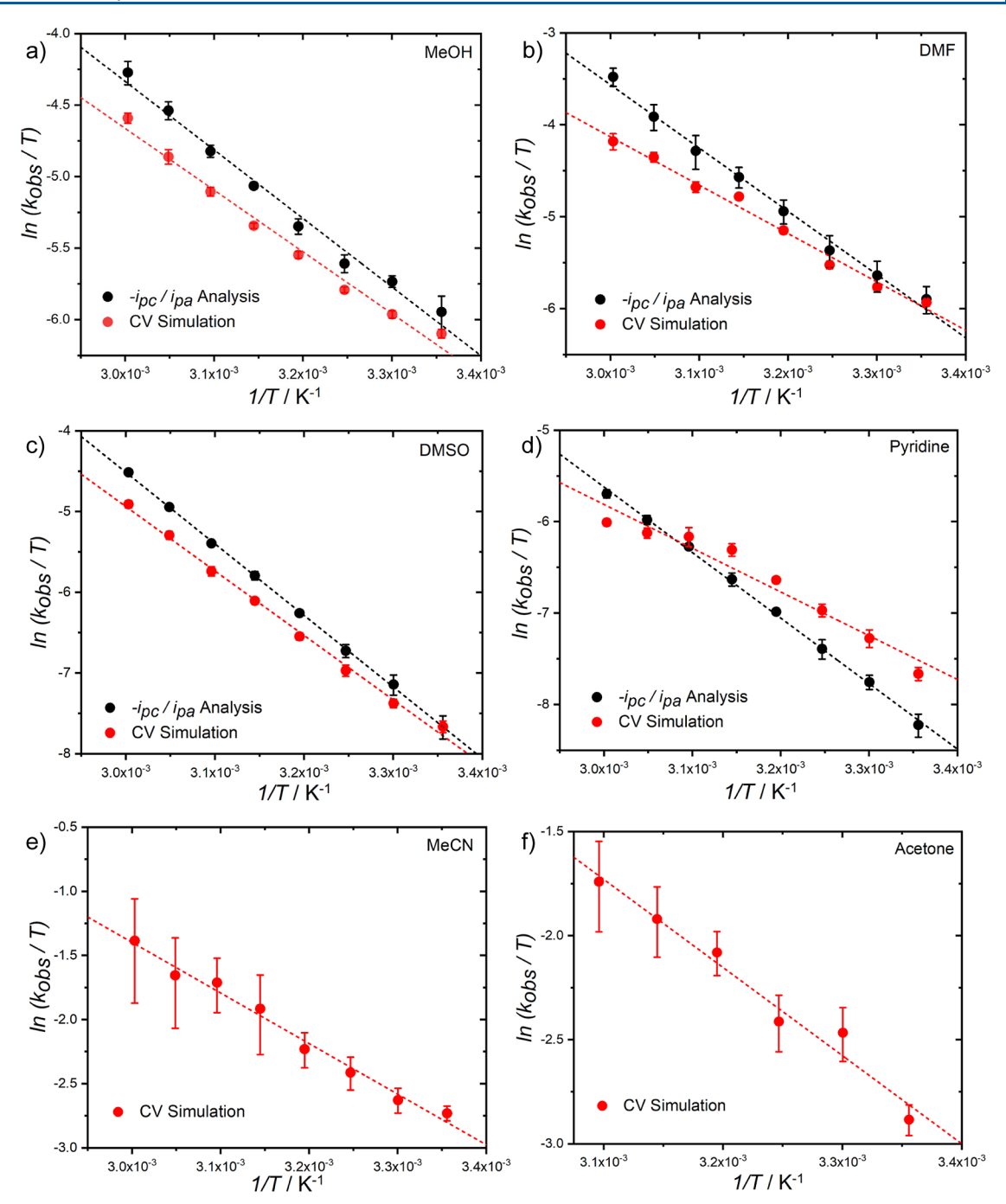


Figure 8. Eyring plots for determination of ΔH_{app}^{\pm} and ΔS_{app}^{\pm} in different solvents. (a) MeOH, (b) DMF, (c) DMSO, (d) Py, (e) MeCN, (f) Ac.

Table 2. Apparent Activation Enthalpies and Activation Entropies Determined for Different Solvents Using $-i_{\rm pc}/i_{\rm pa}$ Analysis^a and CV Simulations^a

solvent	$\Delta H_{\rm app}^{\ \ \pm}/{\rm kJ~mol^{-1}}$		$\Delta S_{\rm app}^{\ \ \ \ \ \ \ \ \ \ \ \ \ \ \ \ \ \ \ $	
	$-i_{\rm pc}/i_{\rm pa}$	CV simulation	$-i_{\rm pc}/i_{\rm pa}$	CV simulation
Ac		35 ± 3		-103 ± 10
MeCN		33 ± 2		-111 ± 5
MeOH	40 ± 2	36 ± 2	-114 ± 6	-128 ± 5
DMF	57 ± 3	44 ± 2	-56 ± 6	-100 ± 5
DMSO	74 ± 1	66 ± 3	-14 ± 1	-39 ± 5
Py	60 ± 1	40 ± 4	-65 ± 3	-126 ± 12

^aError reflects the standard error of the fit to eq 9.

DFT Calculations. To further support the conclusion of competitive dissociative and associative rate limiting steps, DFT calculations were conducted for species proposed to be involved in the C-step for all solvents. All calculations were performed using a 6-31+G* basis set and MN15 functional with a SCRF for each respective solvent. Multiple spin states were interrogated for each structure. Triplet states were found to be the most favorable for structures which included Ni(III), either as monomeric complexes or as dimeric complexes.

Solvent coordination to the $[Ni^{III}(dtc)_2]^+$ species was found to be favorable in all solvents. Figure 11a and Table S5 show summaries of calculated free energies for the formation of solvent coordinated $[Ni^{III}(dtc)_2(sol)]^+$, $trans-[Ni^{III}(dtc)_2(sol)_2]^+$, and $cis-[Ni^{III}(dtc)_2(sol)_2]^+$ structures as

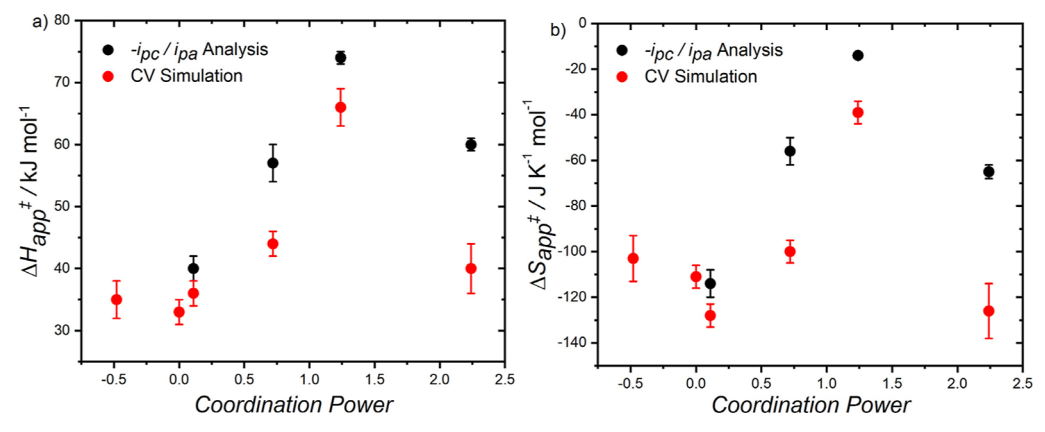


Figure 9. Summary plots for (a) ΔH_{app}^{\dagger} and (b) ΔS_{app}^{\dagger} plotted vs solvent coordination power.

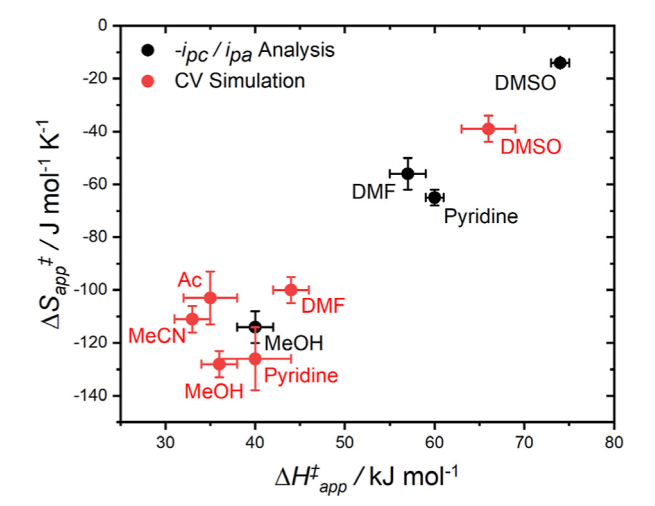


Figure 10. Apparent activation entropy vs apparent activation enthalpy determined for different solvents.

a function of the solvent coordination power. Similar plots are shown in Figure S14 for calculated free energies plotted versus solvent donor number. For Ac, MeCN, and MeOH, the five-coordinate [Ni^{III}(dtc)₂(sol)]⁺ structure was found to be lowest in energy, showing that coordination of a second solvent molecule in either a *cis*- or *trans*-structure was energetically uphill. For the more strongly coordinating solvents of DMF, DMSO, and Py, the formation of six-coordinate complexes was only slightly more favored than the five-coordinate species. Different cis/trans conformations were found to be energetically similar in the case of DMF and DMSO; however, Py exhibited a strong preference for the *cis*-[Ni^{III}(dtc)₂(Py)₂]⁺ structure based on these DFT calculations. We previously reported similar results for Py coordination using an MeCN solvent field.²⁷

A large range of dimer structures involving a combination of $[\mathrm{Ni^{III}}(\mathrm{dtc})_2]^+$, $\mathrm{Ni^{II}}(\mathrm{dtc})_2$, and solvent molecules were also calculated to understand the feasibility of their formation. A total of 41 dimers were considered, of which 7 were found to be thermodynamically stable. Figure 11b and Table S6 provide summaries of their calculated free energies. These seven structures can be grouped into three general families with the structures of each dimer shown in Figure 11c with MeCN coordination for reference and $-\mathrm{N}(\mathrm{Et})_2$ groups removed from the ligands for clarity. Dimer A contains two bridged μ -S atoms with no solvent coordination. This structure is most similar to

reported dithiocarbamate dimers for cobalt and ruthenium. $^{15,35-37}$ Solvent coordination to Dimer A was found to be thermodynamically unfavorable. Dimers B and C represent slip-stacked structures of $[\mathrm{Ni^{III}(dtc)_2}]^+$ and $\mathrm{Ni^{II}(dtc)_2}$ with a single μ -S bridge. The difference in their structures lies in the stacking orientation of the two molecules. Dimer B exhibits a parallel stacking orientation while Dimer C reflects perpendicular stacking. The coordination of a single solvent molecule was found to be favorable for both Dimers B and C with both *cis*- and *trans*-conformations being favorable. Coordination of two solvent molecules to a dimer structure was never found to be thermodynamically stable for any of the calculated dimers.

A comparison of the free energy calculations shown in Figure 11 shows that many dimer structures are lower in energy than solvent coordinated Ni(III) monomers, justifying the thermodynamics for a sequential reaction mechanism in which solvent first coordinates to $[Ni^{III}(dtc)_2]^+$ and then forms a dimer in the second step. Additionally, in all solvents, the ultimate conversion of $[Ni^{III}(dtc)_2]^+$ to $[Ni^{IV}(dtc)_3]^+$ through disproportionation is highly thermodynamically favored (Table S7). Although correlations between activation parameters and transition state energies would be most appropriate, the large number of possible pathways would make this effort exhaustive and less meaningful. Instead, we use the free energy calculations to propose two general pathways to explain the notable dependence of $\Delta H_{\rm app}^+$ on solvent coordination power while balancing the overall associative nature of $\Delta S_{\rm app}^+$.

Path 1 is described by eqs 15 and 16 in which solvent dissociation from the $[Ni^{III}(\bar{d}tc)_2(sol)]^+$ yields $[Ni^{III}(dtc)_2]^+$ which then forms a dimer with Ni^{II}(dtc)₂. We believe Dimer C is the likely product for Path 1 given that it is the most stable of the dimer structures which do not have coordinated solvents. Path 2 is described by eqs 17 and 18 where solvent dissociation occurs from a six-coordinate cis/trans-[Ni^{III}(dtc)₂(sol)₂]⁺ species to yield [Ni^{III}(dtc)₂(sol)]⁺ followed by dimerization with Ni^{II}(dtc)₂ to yield *cis/trans*-Dimer B or *cis/trans*-Dimer C. All solvent coordinated dimers were calculated to be thermodynamically downhill with respect to their solvent coordinated Ni(III) monomers; however, cis-Dimer B was found to be significantly more favorable than other dimers in the case of DMF, DMSO, and Py. Notably for Py, cis-Dimer C was also found to be highly favorable, slightly lower in energy than trans-Dimer B.

Path 1

$$[Ni^{III}(dtc)_2(sol)]^+ \rightarrow [Ni^{III}(dtc)_2]^+ + sol$$
 (15)

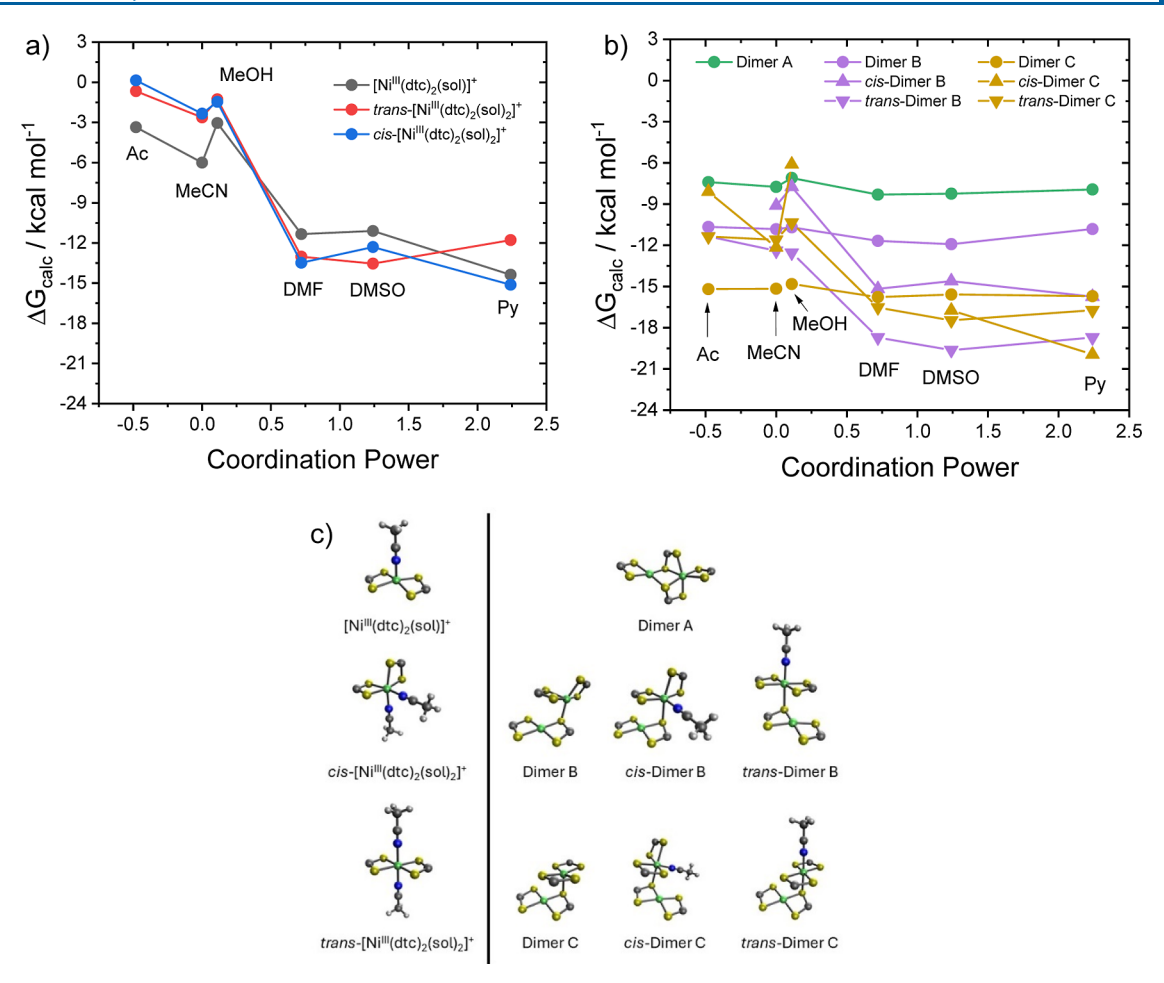


Figure 11. Summary of calculated free energies (ΔG_{calc}) vs solvent coordination power for (a) solvent coordinated Ni(III) complexes and (b) dimer complexes. Note that structures for *cis*-Dimer C in the case of **DMF** and *cis*-Dimer B in the case of **Ac** did not converge to a stable structure and were therefore omitted from the plot. (c) Calculated structures for complexes plotted in parts (a,b) with **MeCN** coordination shown for reference and ligands shown as CS_2^- core with $-N(Et)_2$ groups removed for clarity.

$$[Ni^{III}(dtc)_2]^+ + Ni^{II}(dtc)_2 \rightarrow [Ni_2(dtc)_4]^+$$
 (16)

Path 2

$$\left[\operatorname{Ni}^{\mathrm{III}}(\operatorname{dtc})_{2}(\operatorname{sol})_{2}\right]^{+} \to \left[\operatorname{Ni}^{\mathrm{III}}(\operatorname{dtc})_{2}(\operatorname{sol})\right]^{+} + \operatorname{sol}$$
(17)

$$[Ni^{III}(dtc)_{2}(sol)]^{+} + Ni^{II}(dtc)_{2} \rightarrow [Ni_{2}(dtc)_{4}(sol)]^{+}$$
(18)

Path 1 provides the most straightforward explanation for the increase in $\Delta H_{\rm app}^{+}$ with solvent donor number. As $\Delta G_{\rm calc}$ increased for the formation of $[{\rm Ni^{III}}({\rm dtc})_2({\bf sol})]^+$, so too would the activation barrier for the reverse step, i.e. solvent dissociation. However, Path 2 is also in line with our earlier reports on Py coordination to [Ni^{III}(dtc)₂]⁺ in MeCN solvent.^{25,27} In these studies, we observed an inverse dependence on [Py] in which k_{obs} was found to decrease with higher [Py]. We proposed that this was the result of parallel kinetic pathways in which an equilibrium between mono-Py and bis-Py Ni(III) species allowed the ligand exchange reaction to shift from one path to another as a function of [Pv]. At low [Pv], a kinetically faster ligand exchange was proposed to occur primarily through the mono-Py Ni(III) species while at high [Py], a slower kinetic process occurred through the bis-Py Ni(III) complex. In light of the DFT calculations discussed here, Path 1 is assigned as the faster kinetic path, occurring through [Ni^{III}(dtc)₂(sol)]⁺ while

Path 2 is assigned to the slower kinetic path, occurring through cis/trans-[Ni^{III}(dtc)₂(sol)₂]⁺.

In the case of MeCN, Ac, and MeOH, we believe the DFT calculations support ligand exchange through Path 1. This conclusion is drawn from the result that each of these solvents favors the formation of $[Ni^{III}(dtc)_2(sol)]^+$ as opposed to *cis/* trans- $[Ni^{III}(dtc)_2(sol)_2]^+$. In addition, ΔG_{calc} for Dimer C was found to be lower in energy than all other solvent coordinated dimers for these respective solvents. In the case of DMF, DMSO, and Py, we believe that ligand exchange occurs through Path 2. Strong coordination of these solvents yields favorable thermodynamics for the formation of cis/trans- $[Ni^{III}(dtc)_2(sol)_2]^+$. Furthermore, the formation of solvent coordinated dimers is more thermodynamically favorable than the uncoordinated Dimer C. In summary, DFT calculations support the assignment of two parallel kinetic pathways involving solvent dissociation and dimer formation, one which is favored for more weakly coordinating solvents such as MeCN, Ac, and MeOH and another which is favored for more strongly coordinating solvents such as DMF, DMSO, and Py.

CONCLUSIONS

These results show the impact of solvent coordination on multielectron redox cycles with transition metal complexes. Inherently, any transition metal complex which undergoes

multielectron LCET reactions can be affected by solvent coordination given the fact that an intermediate oxidation state must undergo a change in coordination environment. If the lifetime of the intermediate is long enough, then solvent coordination may impact the two-electron redox path. In the present example, solvent coordination to [Ni^{III}(dtc)₂]⁺ by MeCN and Ac seem to be in a sweet spot which allows them to stabilize the Ni(III) intermediate but dissociate as needed for the ligand exchange reaction to proceed. Notably, the lack of solvent coordination in the case of DCM does not allow for the ECE mechanism to proceed. Finally, we note that in some instances, solvent coordination may even be desired and thus represents the change in coordination environment needed to produce potential inversion. In all cases of multielectron LCET reactions, the role of solvent coordination should be carefully considered.

ASSOCIATED CONTENT

Supporting Information

The Supporting Information is available free of charge at https://pubs.acs.org/doi/10.1021/acs.inorgchem.4c02024.

Cyclic voltammetry, CV simulations, and DFT calculations (PDF)

AUTHOR INFORMATION

Corresponding Author

Byron H. Farnum – Department of Chemistry and Biochemistry, Auburn University, Auburn, Alabama 36849, United States; oorcid.org/0000-0001-9152-1909; Email: farnum@auburn.edu

Authors

Rezoanul Islam — Department of Chemistry and Biochemistry, Auburn University, Auburn, Alabama 36849, United States; orcid.org/0000-0001-9015-0296

Kallan Blakemore – Department of Chemistry and Biochemistry, Auburn University, Auburn, Alabama 36849, United States; oorcid.org/0009-0006-8131-7924

Complete contact information is available at: https://pubs.acs.org/10.1021/acs.inorgchem.4c02024

Notes

The authors declare no competing financial interest.

ACKNOWLEDGMENTS

The work was supported by funding from the National Science Foundation CAREER program under award CHE-1945160.

REFERENCES

- (1) Chang, J.; Bard, A. J. Detection of the Sn (III) intermediate and the mechanism of the Sn (IV)/Sn (II) electroreduction reaction in bromide media by cyclic voltammetry and scanning electrochemical microscopy. *J. Am. Chem. Soc.* **2014**, *136* (1), 311–320.
- (2) Khoshtariya, D. E.; Dolidze, T. D.; Zusman, L. D.; Lindbergh, G.; Glaser, J. Two-Electron Transfer for Tl(aq)³⁺/Tl(aq)⁺ Revisited. Common Virtual [TIII-TIII]⁴⁺ Intermediate for Homogeneous (Superexchange) and Electrode (Sequential) Mechanisms. *Inorg. Chem.* **2002**, *41* (7), 1728–1738.
- (3) Liu, H.; Kuznetsov, A. M.; Masliy, A. N.; Ferguson, J. F.; Korshin, G. V. Formation of Pb (III) intermediates in the electrochemically controlled Pb (II)/PbO2 system. *Environ. Sci. Technol.* **2012**, *46* (3), 1430–1438.

- (4) Gileadi, E. Simultaneous two-electron transfer in electrode kinetics. *J. Electroanal. Chem.* **2002**, 532 (1–2), 181–189.
- (5) Evans, D. H. One-electron and two-electron transfers in electrochemistry and homogeneous solution reactions. *Chem. Rev.* **2008**, *108* (7), 2113–2144.
- (6) Kraiya, C.; Evans, D. H. Investigation of potential inversion in the reduction of 9, 10-dinitroanthracene and 3, 6-dinitrodurene. *J. Electroanal. Chem.* **2004**, *565* (1), 29–35.
- (7) Gosset, A.; Wilbraham, L.; Lachmanová, Š. N.; Sokolová, R.; Dupeyre, G.; Tuyèras, F.; Ochsenbein, P.; Perruchot, C.; de Rouville, H.-P. J.; Randriamahazaka, H.; et al. Electron storage system based on a two-way inversion of redox potentials. *J. Am. Chem. Soc.* **2020**, 142 (11), 5162–5176.
- (8) Bartlett, P. N.; Eastwick-Field, V. A reinvestigation of the electrochemistry of [Ni (II)(bpy) 3 ((ClO) 4) 2] in acetonitrile using rotating disc and rotating ring-disc electrodes. *Electrochim. Acta* **1993**, 38 (17), 2515–2523.
- (9) Sampson, M. D.; Nguyen, A. D.; Grice, K. A.; Moore, C. E.; Rheingold, A. L.; Kubiak, C. P. Manganese catalysts with bulky bipyridine ligands for the electrocatalytic reduction of carbon dioxide: Eliminating dimerization and altering catalysis. *J. Am. Chem. Soc.* **2014**, *136* (14), 5460–5471.
- (10) Jude, H.; Krause Bauer, J. A.; Connick, W. B. An outer-sphere two-electron platinum reagent. *J. Am. Chem. Soc.* **2003**, *125* (12), 3446–3447.
- (11) Lexa, D.; Saveant, J. M. The electrochemistry of vitamin B12. Acc. Chem. Res. 1983, 16 (7), 235–243.
- (12) Liu, W.; Hempstead, M. R.; Nevin, W. A.; Melník, M.; Lever, A. B.; Leznoff, C. C. Disproportionation, electrochemistry, and electronic coupling involving mononuclear and binuclear cobalt phthalocyanine derivatives. *J. Chem. Soc., Dalton Trans.* 1987, No. 11, 2511–2518.
- (13) Lever, A. Electrochemical parametrization of metal complex redox potentials, using the ruthenium(III)/ruthenium(II) couple to generate a ligand electrochemical series. *Inorg. Chem.* **1990**, 29 (6), 1271–1285
- (14) Nair, R. B.; Yeung, L. K.; Murphy, C. J. Synthesis and solvent-dependent properties of ru (acac) 2dppz. *Inorg. Chem.* **1999**, 38 (10), 2536–2538.
- (15) Bond, A.; Martin, R. Electrochemistry and redox behaviour of transition metal dithiocarbamates. *Coord. Chem. Rev.* **1984**, *54*, 23–98.
- (16) Tory, J.; King, L.; Maroulis, A.; Haukka, M.; Calhorda, M. J.; Hartl, F. e. Solvent-Dependent Formation of Os (0) Complexes by Electrochemical Reduction of [Os (CO)(2, 2'-bipyridine)(L) Cl2]; L= Cl-, PrCN. *Inorg. Chem.* **2014**, *53* (3), 1382–1396.
- (17) Kober, E. M.; Sullivan, B. P.; Meyer, T. J. Solvent dependence of metal-to-ligand charge-transfer transitions. Evidence for initial electron localization in MLCT excited states of 2,2'-bipyridine complexes of ruthenium (II) and osmium (II). *Inorg. Chem.* 1984, 23 (14), 2098–2104.
- (18) Leigh, V.; Carleton, D. J.; Olguin, J.; Mueller-Bunz, H.; Wright, L. J.; Albrecht, M. Solvent-dependent switch of ligand donor ability and catalytic activity of ruthenium(II) complexes containing pyridinylidene amide (PYA) N-heterocyclic carbene hybrid ligands. *Inorg. Chem.* **2014**, 53 (15), 8054–8060.
- (19) Cabral, D. M.; Howlett, P. C.; MacFarlane, D. R. Electrochemistry of the tris (2,2'-bipyridine) complex of iron (II) in ionic liquids and aprotic molecular solvents. *Electrochim. Acta* **2016**, 220, 347–353.
- (20) Ershad, S.; Sagathforoush, L.; Karim-Nezhad, G.; Kangari, S. Electrochemical behavior of N2SO Schiff-base Co (II) complexes in non-aqueous media at the surface of solid electrodes. *Int. J. Electrochem. Sci.* **2009**, 4 (6), 846–854.
- (21) O'Toole, T. R.; Younathan, J. N.; Sullivan, B. P.; Meyer, T. J. 1, 2-Difluorobenzene: a relatively inert and noncoordinating solvent for electrochemical studies on transition-metal complexes. *Inorg. Chem.* **1989**, 28 (20), 3923–3926.

- (22) Kapturkiewicz, A.; Behr, B. Solvent effect on electrode reaction kinetics of transition metal salene complexes. *J. Electroanal. Chem. Interfacial Electrochem.* **1984**, 179 (1–2), 187–199.
- (23) Lachenal, D. Electrochemical behaviour of nickel (II) and Ni (IV) N, N-diethyldithiocarbamates. Synthesis of a nickel (IV) species. *Inorg. Nucl. Chem. Lett.* **1975**, *11* (2), 101–106.
- (24) Hendrickson, A.; Martin, R.; Rohde, N. Dithiocarbamates of nickel in the formal oxidation states I-IV. Electrochemical study. *Inorg. Chem.* **1975**, *14* (12), 2980–2985.
- (25) Richburg, C. S.; Farnum, B. H. Influence of Pyridine on the Multielectron Redox Cycle of Nickel Diethyldithiocarbamate. *Inorg. Chem.* **2019**, *58* (22), 15371–15384.
- (26) Mazumder, M. M. R.; Dalpati, N.; Pokkuluri, P. R.; Farnum, B. H. Zinc-Catalyzed Two-Electron Nickel (IV/II) Redox Couple for Multi-Electron Storage in Redox Flow Batteries. *Inorg. Chem.* **2022**, *61* (48), 19039–19048.
- (27) Mazumder, M. M. R.; Burton, A.; Richburg, C. S.; Saha, S.; Cronin, B.; Duin, E.; Farnum, B. H. Controlling One-Electron vs Two-Electron Pathways in the Multi-Electron Redox Cycle of Nickel Diethyldithiocarbamate. *Inorg. Chem.* **2021**, *60* (17), 13388–13399.
- (28) Savéant, J.-M. Elements of Molecular and Biomolecular Electrochemistry: An Electrochemical Approach to Electron Transfer Chemistry; John Wiley & Sons, 2006.
- (29) Kaur, R.; Dalpati, N.; Delcamp, J. H.; Farnum, B. H. Nickel-Based Two-Electron Redox Shuttle for Dye-Sensitized Solar Cells in Low Light Applications. *ACS Appl. Energy Mater.* **2024**, *7* (9), 3645–3655.
- (30) Frisch, M. e.; Trucks, G.; Schlegel, H. B.; Scuseria, G.; Robb, M.; Cheeseman, J.; Scalmani, G.; Barone, V.; Petersson, G.; Nakatsuji, H. *Gaussian 16*; Gaussian, Inc.: Wallingford, CT, 2016.
- (31) Munakata, M.; Kitagawa, S.; Miyazima, M. Classification of solvents based on their coordination power to nickel (II) ion. A new measure for solvent donor ability. *Inorg. Chem.* **1985**, 24 (11), 1638–1643
- (32) Gutmann, V. Solvent effects on the reactivities of organometallic compounds. *Coord. Chem. Rev.* **1976**, 18 (2), 225–255.
- (33) Carnes, M.; Buccella, D.; Chen, J.; Ramirez, A. P.; Turro, N. J.; Nuckolls, C.; Steigerwald, M. A stable tetraalkyl complex of nickel (IV). *Angew. Chem.* **2009**, *121* (2), 296–300.
- (34) Dimitrov, V.; Linden, A.; Pseudotetrahedral, A. High-Oxidation-State Organonickel Compound: Synthesis and Structure of Bromotris (1-norbornyl) nickel (iv). *Angew. Chem.* **2003**, *115* (23), 2735–2737
- (35) Bond, A. M.; Colton, R.; Ho, Y.; Moir, J.; Page, D.; Stott, R. Characterization of pentakis (dithiocarbamato) dicobalt(III) complexes,[Co₂(RR'dtc)₅]⁺, and related complexes in dichloromethane using electrochemical and cobalt-59 NMR techniques. *Inorg. Chem.* **1985**, 24 (25), 4402–4407.
- (36) Mattson, B.; Heiman, J.; Pignolet, L. Oxidation of tris(N,N-disubstituted-dithiocarbamato) complexes of ruthenium(III). X-ray structure determination of bis(N,N-diethyldithiocarbamato)-.mu-tris(N,N-diethyldithiocarbamato)-diruthenium(III) tetrafluoroborate, [Ru₂(Et₂dtc)₅] BF₄. *Inorg. Chem.* 1976, 15 (3), 564–571.
- (37) Hendrickson, A. R.; Martin, R. L.; Taylor, D. Synthesis and properties of dimeric cobalt (III) dithiocarbamate complexes $[\text{Co}_2(\text{R}_2\text{dtc})_5]^+$: X-ray structural analysis of pentakis (diethyldithiocarbamato) dicobalt (III) tetrafluoroborate. *J. Chem. Soc., Dalton Trans.* 1975, No. 21, 2182–2188.